Analyst

Quantitative Imaging of the Sub-Organ Distributions of Nanomaterials in Biological Tissues via Laser Ablation Inductively Coupled Plasma Mass Spectrometry

Journal:	*Analyst*
Manuscript ID	AN-ART-05-2023-000839.R1
Article Type:	Paper
Date Submitted by the Author:	22-Jul-2023
Complete List of Authors:	Jantarat, Teerapong; University of Massachusetts, Department of Chemistry Lauterbach, Joshua; University of Massachusetts, Department of Chemistry Doungchawee, Jeerapat; University of Massachusetts Amherst, Chemistry Agrohia, Dheeraj; University of Massachusetts, Department of Chemistry Vachet, Richard; University of Massachusetts, Department of Chemistry

Quantitative Imaging of the Sub-Organ Distributions of Nanomaterials in Biological Tissues via Laser Ablation Inductively Coupled Plasma Mass Spectrometry

Teerapong Jantarat, Joshua D. Lauterbach, Jeerapat Doungchawee, Dheeraj K. Agrohia, Richard W. Vachet*

Department of Chemistry, University of Massachusetts, 710 North Pleasant Street, Amherst, MA 01002, USA

*Corresponding author: rwvachet@chem.umass.edu

Abstract

Nanomaterials have been employed in many biomedical applications, and their distributions in biological systems can provide an understanding of their behavior *in vivo*. Laser ablation inductively coupled plasma mass spectrometry (LA-ICP-MS) can be used to determine the distributions of metal-based NMs in biological systems. However, LA-ICP-MS has not commonly been used to quantitatively measure the cell-specific or sub-organ distributions of nanomaterials in tissues. Here, we describe a new platform that uses spiked gelatin standards with control tissues on top to obtain an almost perfect tissue mimic for quantitative imaging purposes. In our approach, gelatin is spiked with both nanomaterial standards and an internal standard to improve quantitation and image quality. The value of the developed approach is illustrated by determining the sub-organ distributions of different metal-based and metal-tagged polymeric nanomaterials in mice organs. The LA-ICP-MS images reveal that the chemical and physical properties of the nanomaterials cause them to distribute in quantitatively different extents in spleens, kidneys, and tumors, providing new insight into the fate of nanomaterials *in vivo*. Furthermore, we demonstrate that this approach enables quantitative co-localization of nanomaterials and their cargo. We envision this method being a valuable tool in the development of nanomaterial drug delivery systems.

Introduction

Nanomaterials (NMs) are employed for several purposes in biomedical applications, including early diagnosis, therapeutics, and drug delivery.[1] Metal-based NMs are commonly used because of their attractive properties.[2] For example, they are easy to synthesize; they have tunable sizes and shapes; and their surfaces can be readily modified with various ligands to impart targeting capability.[3] Given their importance in biomedical applications, tracking NMs in biological systems is crucial for understanding their behavior or mechanisms of action. Furthermore, obtaining cell-specific and sub-organ quantitative information about NMs *in vivo* is important for the optimal development of NM-based drug delivery platforms, so that their biological transport and fate in heterogeneous organs can better understood.

Several techniques have been used for tracking the locations of NMs in biological samples. Fluorescence microscopy is perhaps the most commonly used method to image the location of NMs in biological systems. This technique exhibits high-spatial resolution, allows live cell imaging, and can be used to monitor NMs in tissues. Fluorescence measurements often require the NMs to be tagged in some way to emit fluorescence,[4,5] and typically only a few fluorophores can be measured at a time, which can limit its multiplexing capability. Most importantly, quantitative information can be difficult to obtain.[6] Transmission electron microscopy (TEM) allows visualization of NMs with high resolution, but it does not readily provide quantitative information because it is challenging to measure all the NMs in a sample by TEM.

Laser ablation inductively coupled plasma mass spectrometry (LA-ICP-MS) has emerged as a powerful tool for tracking the distribution of metal-based NMs in biological systems.[7] [8]This technique provides several advantages over other techniques, such as multi-element detection capability and high sensitivity, while not requiring NMs to be tagged.[9] Furthermore, it has excellent quantitative ability when the sample is fully ablated, atomized, and detected.[10] Successful quantitative imaging using LA-ICP-MS requires the use of matrix-matched standards to mimic the properties of biological samples. Several approaches to matrix matching have been developed. Perhaps the most common method is the use of tissue homogenates that are spiked with the analyte of interest. This method, however, is often less than ideal due to heterogeneous distributions of the standards and uneven surface roughness after cryo-sectioning that can result imprecise quantitative information.[11–14] Another approach is to use polymeric thin films, such as PMMA,[15] agarose,[16] paper,[17] and gelatin[18] that are spiked or ink-jet printed with the analyte standards of interest. While typically providing more homogeneous distributions of analyte standards and smooth surfaces, these types of standards do not always appropriately mimic the properties of all biological tissue types.

Another issue that can be confronted in quantitative LA-ICP-MS imaging experiments is signal drift, especially during long imaging experiments, which can lead to poor quantitation if not accounted for. A few approaches have been used to overcome this problem. For instance, the element signal of interest can be normalized to a naturally existing element in the tissues, such as Zn or ^{13}C to obtain a more reliable LA-ICP-MS image.[19,20] However, any variations in the levels of the naturally existing element leads to incorrect normalization.[21] Another approach has been to use metal-doped (e.g. In) commercial inks that are printed on top of the tissue sections.[22 23] However, this method can sometimes cause changes to the tissue sample.

In this manuscript, we present a new method based on LA-ICP-MS imaging that allows the sub-organ distributions of NMs in tissues to be readily quantified. LA-ICP-MS has been used for the quantitative imaging of NMs in biological tissues, typically using spiked tissue homogenates for matrix-matched standards;[24–26] however, quantitative information in specific sub-organ regions is not usually determined by LA-ICP-MS. The method presented here uses a thin layer of gelatin underneath control tissues as a matrix-matched standard. Gelatin is easy to prepare in homogeneous thin layers (< 10 μm), has tissue-like properties, and can be readily spiked with standards for quantitation and elements to correct for any signal drift. While gelatin has been used previously as a matrix-matched standard for quantitative LA-ICP-MS imaging,[18,27,28] our approach places control tissue sections of interest on top of spiked gelatin to render an almost perfect biological tissue mimic, regardless of the tissue material. We demonstrate that this matrix-matching platform enables the quantification of NMs in the sub-organ regions of a variety of tissue types, obtaining information that will allow us to better understand NM behaviors *in vivo*.

Experimental section

1. Nanomaterial synthesis

All NMs used in this work are shown in Figure S1. The gold nanoparticles (AuNPs) used in this work were synthesized using the Brust–Schiffrin two phase method.[29] These AuNPs contain a Au core consisting of approximately 200 atoms and a surface of self-assembled monolayers that maintain their stability, biocompatibility and surface chemistry. Two different ligands were used for the monolayers, one terminated with a positively-charged alkylammonium group (TTMA) and another terminated with a negatively-charged carboxylate group (TEGCOOH). The syntheses of the TTMA and TEGCOOH ligands and corresponding AuNPs have been described previously.[30,31] AuNP-based nanozymes were synthesized using published procedures,[32] including encapsulation with an organopalladium catalyst.[33] Polymeric nanomaterials (PNMs)

composed of a guanidinium functionalized polyoxanorborneneimide (PONI) polymer (molecular weight: 60 kDa) together with green fluorescent protein (GFP) cargo were also studied. The PONI polymer and GFP were conjugated with a 1,4,7,10-tetraazacyclododecane-1,4,7,10- tetraacetic acid (DOTA) ligand to enable metal tagging, as described previously.[34] The polymer-DOTA conjugate was loaded with Tb metal ions, and the GFP-DOTA conjugate was loaded with Tm metal ions. These polymer-protein nanocomposites were synthesized and assembled using published protocols.[35,36] Dynamic light scattering and zeta potential measurements were conducted to characterize all the resulting nanomaterials, and the results are shown in Table S1.

2. Preparation of spiked gelatin standards

A mold for the gelatin was prepared by placing 50-μm thick Teflon™ tape on a glass slide and then cutting the tape to create thin wells into which the spiked-gelatin standards were placed (Figure S2). Gelatin from porcine skin (Sigma-Aldrich, St. Louis, MO, USA) was dissolved in Milli-Q water and heated to 80 ^{0}C. Then, $HoCl_3$ (Sigma-Aldrich, St. Louis, MO, USA) as an internal standard was stirred into the gelatin solution until a homogenous solution was obtained. Standards of the NMs of interest were prepared at the desired concentrations in separate vials, and then the hot gelatin solution was added to these vials and sonicated at 60 ^{0}C for 15 min. The spiked gelatin standards were then added into the prepared mold, and the excess gelatin was removed using a glass coverslip. The spiked gelatin standards on the mold were allowed to solidify at -20 ^{0}C for 15 min. Gelatin concentrations of 7.5, 10.0, 12.5 and 15.0% w/v were investigated. The thickness and roughness of the resulting gelatin layers were measured using an Alpha-Step D-500 Stylus profilometer (KLA Tencor, Milpitas, CA, USA).

3. Animal experiments and tissue preparation for imaging

Balb/c mice samples were injected with the NM of interest and euthanized after 0.5 h, 1 day, 6 days, or 10 days. The AuNPs and polymeric NMs were injected intravenously, and the nanozymes were injected directly into the tumors of tumor-bearing mice. Mice were sacrificed by carbon dioxide inhalation and cervical dislocation. All animal experiments were approved by the University of Massachusetts Institutional Animal Care and Use Committee, which is guided by the U.S. Animal Welfare Act and U.S. Public Health Service Policy. After collection, the tissue samples were flash frozen and stored at -80 ^{0}C until ready for sectioning. To prepare the tissue section for the imaging experiments, the tissues were sliced to a thickness of 12 μm using a Leica CM1850 cryostat at -20 ^{0}C. Then, the sectioned tissues of interest were placed on top of gelatin

containing only spiked Ho. Also, control tissue sections from mice injected with saline alone were placed on top of spiked gelatin standards containing different concentration of the NM of interest.

4. LA-ICP-MS optimizations and conditions.

The sample glass slides, containing the tissue sections on top of gelatin, were placed in the ablation cell of a CETAC LSX-213 G2 laser ablation system (Photon Machines, Omaha, NE, USA) that was connected to a Perkin Elmer NexION 300x ICP-MS (Waltham, MA, USA). Several laser ablation parameters were optimized to ensure complete ablation of the tissue and underlying gelatin layer. These parameters included the laser energy, laser power, laser speed rate, and the carrier gas flow. The laser spot size was fixed at 100 µm in all imaging experiments. The optimal laser energy was found to be 3.34 J/cm^2 with 70% laser power. The laser scan rate was selected to be 20 µm s^{-1} with a 10 s shutter delay. Helium gas was used as a carrier gas, and the optimal flow rate was found to be 0.8 L min^{-1}. Other ICP-MS experimental parameters were identical to those used in previous LA-ICP-MS work on nanomaterials.[24,37,38] The washout time of the laser ablation system was 500 ms. The isotopes used to measure the elements of interest were ^{57}Fe, ^{106}Pd, ^{158}Tb, ^{165}Ho, ^{169}Tm, and ^{197}Au. A 50 ms dwell time was used for the detection of all isotopes.

5. Data analysis and image generation

For the calibrations, each spiked standard was ablated to a length of 600 µm, and the data were converted to an image using a custom Python script. The NM metal signal of interest was normalized to the Ho signal for each standard, and a calibration plot between the normalized signal and NM concentrations was generated. Data from the LA-ICP-MS experiments were reconstructed into images, analyzed, quantified, and segmented using the Python script RecSegImage-LA,[19] which is freely available at GitHub (https://github.com/Vachet-Lab/RecSegImage-LA). In some cases, as indicated below, hotspot removal was performed to improve the visual appearance of the image, allowing for a clearer depiction of element distributions in the tissues. Hotspot removal was not used for any quantitation. Hotspot removal was accomplished by selecting the ion signals in > 0.99 quantile and replacing them with the 0.99 quantile value, as done previously.[39,40]

Results and discussion

1. Experimental design and gelatin standard preparation

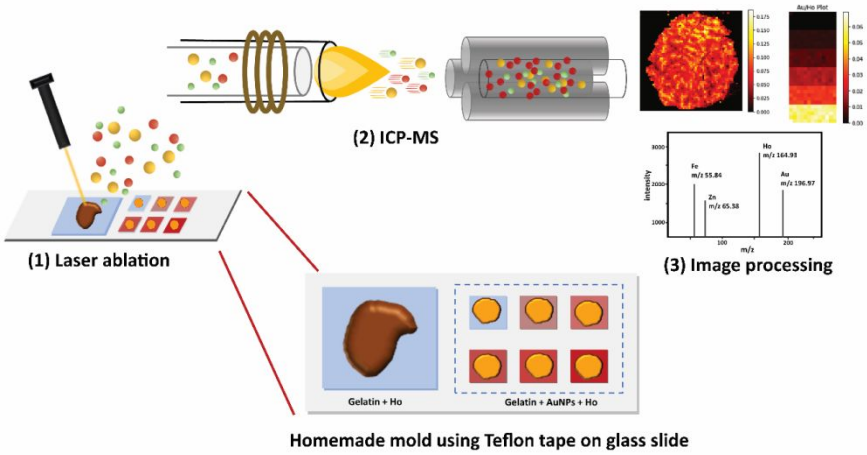

Figure 1. Schematic illustration of the steps involved in the quantitative imaging of a biological sample using spiked gelatin standards. (1) The sample is placed on top of a thin layer of gelatin spiked with an internal standard, and laser ablation is performed; (2) ICP-MS is used for detection of the ablated material; (3) Data processing with RecSegImage-LA[19] is used for image reconstruction and quantitation.

Gelatin has several properties that make it an effective matrix-matched standard material, including its ease of preparation, inherent homogeneity, and tissue like morphology. Standards can also be homogeneously incorporated into gelatin as it starts as a liquid before solidifying upon cooling. Our general approach was to cryo-section the tissue of interest and place it on top of a thin layer of gelatin containing an internal standard (i.e. Ho). Six control tissues of the same organ were also sectioned and placed on top of thin layers of gelatin that were spiked with an internal standard and calibration standards of the NMs. The tissues were then analyzed by the LA-ICP-MS system (Figure 1), and NM signals were normalized to the Ho signal to account for any signal drift or variations in laser intensity during the sometimes long (>8 h) imaging experiments.

The preparation of the spiked gelatin standards was optimized to ensure quantitative reproducibility and to generate layers that did not deleteriously impact NM ablation and detection in the tissues of interest. During optimization of the gelatin layer, we found that 7.5% w/v of gelatin cooled to a temperature of -20 ^{0}C and spiked with 50 µg/g of Ho produced thin (~ 3-4 µm) and smooth (Figure S3) layers that yielded homogeneous (Figure S4), sensitive (Figure S5), and reproducible calibration standards (Figure S6 and Table S2). In addition, we found that five 600-µm long ablation lines for each calibration standard provided reliable and reproducible imaging signals for quantitation (Figure S7) without sacrificing too much analysis time (Table S3). We also tested the reproducibility of the spiked gelatin preparation. Six different batches of the spiked gelatin standards were prepared, and these spiked gelatin standards were analyzed on six

different days over the course of two months to assess the reproducibility of the gelatin standard preparation. Figure S8 shows that the resulting calibration sensitivities have a relative standard deviation (RSD) of only 8.0% over this time, indicating that this preparation method is robust and reproducible.

2. The improvement of the quantitative analysis and image quality

As compared to conventional spiked tissue homogenates, the spiked gelatin standards with control tissues on top provide less signal fluctuation (Figure 2). The conventional tissue homogenates were prepared as previously described[24] by spiking AuNPs and Ho into homogenized beef liver that was then frozen and sectioned to a thickness of 12 µm. The optical images and the LA-ICP-MS signals of spiked gelatin standards with control tissues on top show a much smoother surface (Figure 2A) and more consistent signal (Figure 2B) than the tissue homogenate standard. The gelatin standards also improve pixel homogeneity (Figure 2C) and the reproducibility of the calibration plots (Figure 2D) with the RSDs ranging from 2 to 9% for the spiked gelatin standards as opposed to 13 to 26% for the conventional tissue homogenates. It should be noted that the presence of the tissue section on top of the gelatin does not signficantly affect the signal sensitivity (Figure S7C). An additional advantage of spiking Ho into the gelatin underlayer is to correct for variations in laser intensity that sometimes occur during LA-ICP-MS

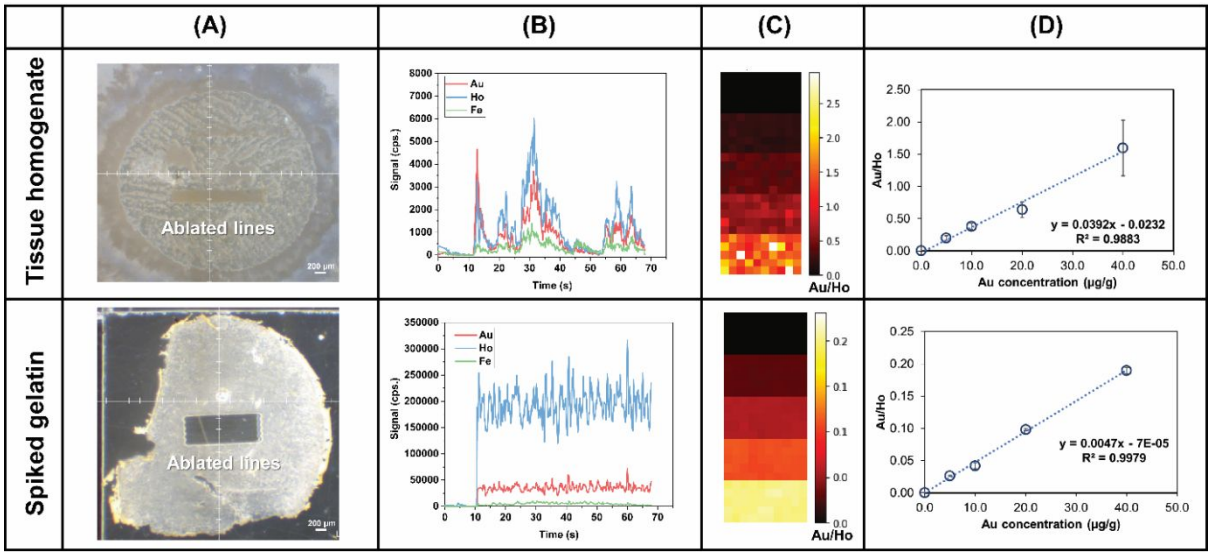

Figure 2. LA-ICP-MS imaging results obtained from a beef liver homogenate section (top) and a control tissue on top of a spiked gelatin standard (bottom). (A) Optical images of the spiked matrix-matched standards. (B) Example signal from LA-ICP-MS analysis, showing the metal signals detected across a single scanned line. (C) Au signal from five 600-µm long ablation lines normalized by the Ho signal. (D) The calibration plot between Au/Ho signal vs. Au concentration. TTMA AuNPs were the NMs used in these experiments.

analyses of calibration standards (e.g. Figure S9). The gelatin-based calibration curve in Figure 2 allows us to estimate the per pixel limit of detection (LOD) and limit of quantitation (LOQ) for our imaging approach. We find the LOD and LOQ for the AuNPs to be 0.18 μg/g and 0.21 μg/g, respectively.

Utilizing Ho as an internal standard in the gelatin layer also can improve the quality of poor LA-ICP-MS images that have significant fluctuations due to signal drift or laser intensity variations. Figure 3 shows the reconstructed image of a spleen section taken from a mouse 1 day after being

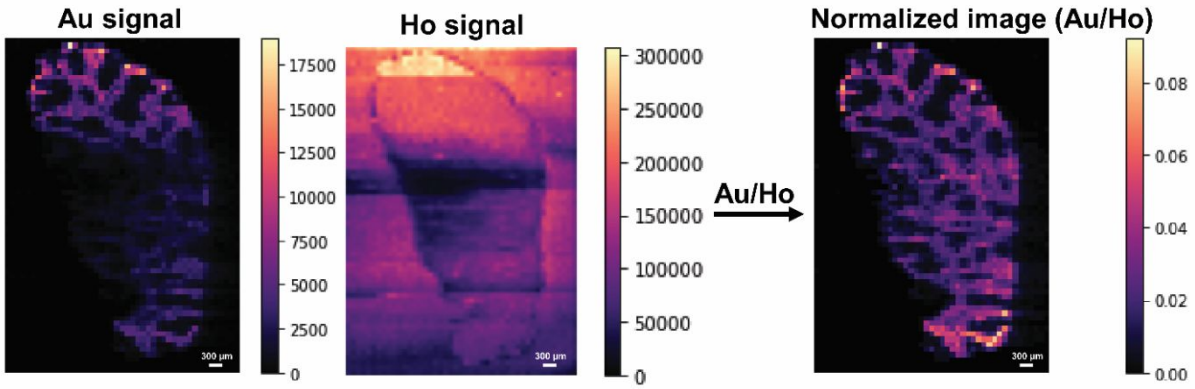

Figure 3. LA-ICP-MS image quality can be improved by utilizing Ho signals for normalization. Au signals in a spleen section from a mouse injected with TEGCOOH AuNPs vary across the tissue section due to signal drift and/or laser energy fluctuations. The resulting image can be improved by normalizing to the Ho signal that is present in the gelatin underlayer.

injected with TEGCOOH AuNPs. Variations in the Au signal due to fluctuations in the laser energy render an inconsistent image due to fluctuations in the Au signal. These fluctuations are also present in the Ho signal, despite a homogeneous distribution of Ho in the gelatin underlayer (e.g. see a typical Ho distribution in Figure S10). When the Au signal is normalized to the Ho signal, a corrected image can be obtained (Figure 3).

Upon using the gelatin standards spiked with Ho and the NM of interest, as illustrated in Figure 1, we are able to obtain images that provide the quantitative distributions of NMs in different

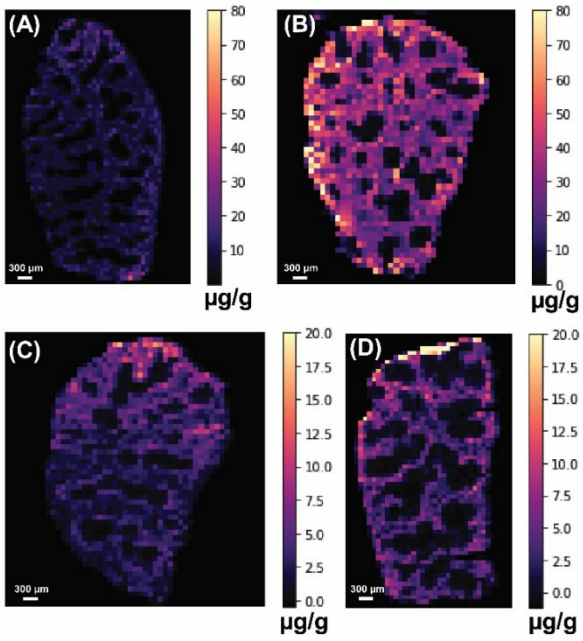

Figure 4. Quantitative distributions of AuNPs in spleen sections from mice injected with different AuNPs. (A) Spleen tissue section from a mouse one day after being injected with TTMA AuNPs. (B) Spleen tissue section from a mouse six days after being injected with TTMA AuNPs. (C) Spleen tissue section from a mouse one day after being injected with TEGCOOH AuNPs. (D) Spleen tissue section from a mouse six days after being injected with TEGCOOH AuNPs.

tissue sections. Figure 4 shows four spleen sections taken one and six days after mice were injected with either TTMA AuNPs or TEGCOOH AuNPs. These images reveal that Au from the NMs is heterogeneously distributed in the spleen. Such a heterogeneous distribution of Au would not be evident from the analyses of spleen homogenates, exemplifying the value of LA-ICP-MS imaging. The images also reveal that more Au accumulates in the spleen of mice injected with the TTMA AuNPs than mice injected with the TEGCOOH AuNPs. Moreover, the Au signal increases more extensively in the spleen six days after injection of the TTMA AuNPs, as indicated by the brighter color in Figure 4, than it does six days after injection of the TEGCOOH AuNPs.

To validate these quantitative imaging results, we compared the quantities obtained from LA-ICP-MS analysis to ICP-MS results from homogenates of the same spleen samples. To make this comparison, the spleen tissues were cut into two parts. One part of the tissue was digested and analyzed by ICP-MS, and the other part (~ 10 % of the tissue) was sliced into at least three different 12-µm sections and quantitatively imaged by LA-ICP-MS. The average Au concentrations across all the pixels from three tissue sections were then compared to the Au

concentrations obtained from ICP-MS analysis of the digested tissues. The results are in reasonable agreement as shown in Table 1, with accuracies ranging between 55 and 90%, suggesting that our quantitative imaging approach is reliable. It should be noted that the error bars associated with the LA-ICP-MS analyses are generally higher as would be expected since only a small section of the organ is analyzed.

Table 1. Comparison of LA-ICP-MS quantitative results of spleen tissue sections with ICP-MS results of homogenized and digested spleen tissues, validating the quantitative accuracy of LA-ICP-MS when gelatin standards are used.

Sample	ICP-MS (ng/g)	LA-ICP-MS (ng/g)
Day 1 (TTMA AuNPs)	15000 ± 1000[a]	12000 ± 2000[b]
Day 6 (TTMA AuNPs)	33000 ± 2000[a]	30000 ± 20000[c]
Day 1 (TEGCOOH AuNPs)	4000 ± 1000[a]	3000 ± 1000[b]
Day 6 (TEGCOOH AuNPs)	7200 ± 300[a]	4000 ± 1000[b]

[a] The error bars are standard deviations (n = 3) that are obtained from ICP-MS analysis of three replicate measurements.
[b] The error bars are standard deviations (n = 3) that are obtained by averaging the quantitative LA-ICP-MS results obtained from three different tissue sections from mice injected with the indicated AuNP.
[c] The error bars are standard deviations (n = 4) that are obtained by averaging the quantitative LA-ICP-MS results obtained from four different tissue sections from mice injected with the indicated AuNP.

3. Quantitative sub-organ distributions of nanomaterials

The real value of our imaging approach is the ability to determine the NM quantities in distinct sub-organ regions. Quantitative information about NM distributions in different cell types of organs such as the kidney, liver, or spleen can provide new insight into the excretion of these NMs and their interactions with the immune system. As an initial proof of principle, we investigated how the polarity of AuNP surface charge influences their quantitative distribution in different regions of the spleen. NMs often accumulate at high levels in the spleen, and their distributions in different regions (i.e. red pulp, white pulp, and marginal zone) provide insight into how NMs are filtered from the blood and interact with the immune system.[41] The heterogeneous distributions of Au found in the spleen (i.e. Figure 4) can be correlated to the red pulp and white pulp regions via image segmentation using the Fe signal, which is measured at the same time

as the Au and Ho signals. The Fe signal is higher in the red pulp than the white pulp due to the high concentration of hemoglobin as red blood cells are filtered by the red pulp of the spleen. The white pulp is a reservoir of immune-system related lymphocytes and has lower levels of Fe. Segmentation was performed on the Fe distributions using a *k*-means clustering protocol in RegSegImage,[19] and an example is shown in Figure 5. The segmentation process allows every pixel in the LA-ICP-MS image to be classified as either red pulp, white pulp, or background (i.e. outside the tissue boundary). When the Au amounts in each pixel are thus classified, the quantities of Au in the red and white pulp can be determined (Table 2). Segmentation of the LA-ICP-MS images for spleen sections from mice injected with TTMA AuNPs or TEGCOOH AuNPs indicate that both the positively and negatively-charged AuNPs accumulate to a greater extent in the red pulp of the spleen than in the white pulp. Interestingly, the quantitative information in the sub-organ regions of the spleen reveals the significant increase of the TTMA AuNPs occurs equally in both the red pulp and white pulp over a period of six days after the injection of this AuNP (Table 2). In contrast, the amount of the TEGCOOH AuNPs does not increase significantly in the white pulp after six days (Table 2), suggesting these AuNPs interact differently with the immune system. Such new information would not be available from ICP-MS analyses of spleen homogenates but is readily available from quantitative LA-ICP-MS imaging.

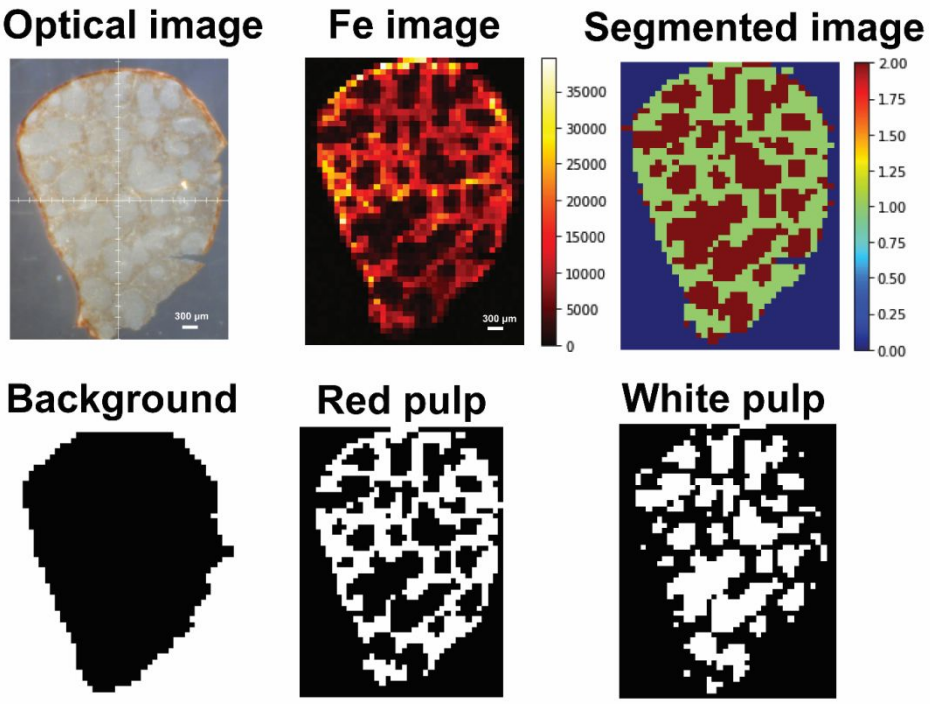

Figure 5. Example optical, LA-ICP-MS, and segmented images of a spleen section taken from a mouse six days after being injected with TEGCOOH AuNPs. Segmentation of the Fe distributions from the LA-ICP-MS imaging analysis was accomplished using RegSegImage[19] and allows each pixel to be classified as background, red pulp, or white pulp.

Table 2. Total AuNP concentrations in the spleen and in the red and white pulp sub-organ regions from LA-ICP-MS analyses.

Sample	Au (ng/g)		
	Total	Red pulp	White pulp
Day 1 (TTMA AuNPs)	12000 ± 2000[a]	8000 ± 700[a]	4000 ± 2000[a]
Day 6 (TTMA AuNPs)	30000 ± 20000[b]	20000 ± 10000[b]	11000 ± 5000[b]
Day 1 (TEGCOOH AuNPs)	3000 ± 1000[a]	2000 ± 500[a]	1000 ± 500[a]
Day 6 (TEGCOOH AuNPs)	4000 ± 700[a]	3000 ± 1000[a]	1100 ± 200[a]

[a] The error bars are standard deviations (n = 3) that are obtained by averaging the quantitative LA-ICP-MS results obtained from three different tissue sections from mice injected with the indicated AuNP.

[b] The error bars are standard deviations (n = 4) that are obtained by averaging the quantitative LA-ICP-MS results obtained four different tissue sections from mice injected with the indicated AuNP.

To illustrate the multiplexed quantitative ability of our approach, we next investigated AuNPs that have a bioorthogonal palladium catalyst embedded in their monolayer to create a nanozyme that can transform therapeutically inactive molecules, or pro-drugs, into active drugs *in vivo*.[42] The nanozymes were injected directly into breast cancer tumors that had been implanted, and the mice were sacrificed 10 days after injection of the nanozymes. The tumor was excised and sliced into two perpendicular sections as shown in Figure S11, and the tumor sections were placed on top of the spiked gelatin. Three adjacent tissue sections were analyzed for Au, Pd, Fe, and Ho by LA-ICP-MS. Based on calibration curves for these nanozyme samples, the per pixel LOD and LOQ values for the AuNPs are 0.84 μg/g and 0.91 μg/g, respectively, whereas the LOD and LOQ of Pd in the nanozyme samples were 0.39 μg/g and 0.44 μg/g, respectively.

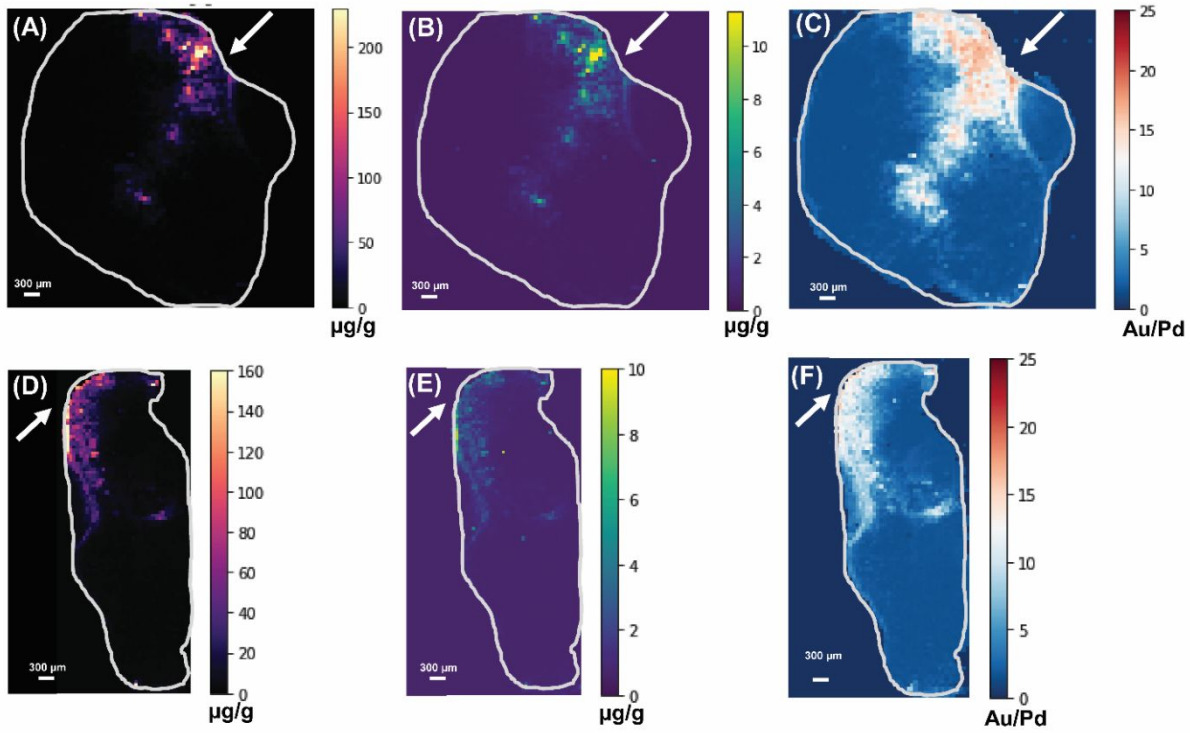

Figure 6. Quantitative distributions of Au and Pd in mouse tumor sections from LA-ICP-MS imaging after injection of a AuNP-based nanozyme. The tumor was sectioned into two different perpendicular dimensions (see Figure S10). (A) Quantitative image of Au from a tumor section in one of the dimensions. (B) Quantitative image of Pd from the same tumor section as in (A). (C) Ratiometric image of Au/Pd signals from the tumor section shown in (A) and (B). (D) Quantitative image of Au from a tumor section that was sliced perpendicular to section shown in (A) and (B). (E) Quantitative image of Pd from the same tumor section shown in (D). (F) Ratiometric image of Au/Pd signals from the tumor section shown in (D) and (E).

The resulting images reveal several important aspects about the nanozyme distributions. First, Au and Pd have the same distribution as shown in Figure 6. From the site of injection, the Au and Pd signals radiate out in three dimensions as can be seen from the sets of images in Figure 6A, B, D, and E. When the Au and Pd levels are correlated on a pixel-by-pixel basis using Pearson correlation coefficients, we find that the two elements are distributed almost identically in the tumor sections with correlations of 0.998 and 0.995 for the two sets of images. These results indicate that the AuNPs and Pd catalyst remain together and intact *in vivo* for at least 10 days after injection. Second, we considered the ratio of the Au and Pd quantities from the LA-ICP-MS images and compared them to the initial injection ratio. When considering the quantitative Au/Pd ratios for all the pixels in the images, we find average values of 11 ± 5 and 12 ± 2, respectively, for the two sets of images in Figure 6, which are comparable to the initial injection ratio of 12.9 ± 0.5. The Au/Pd ratiometric images shown in Figures 6C and 6F illustrate that Au and Pd signals are close to the injected ratio in most of the pixels

throughout the tumor tissue as indicated by the white pixels. Lastly, the nanozymes spread out in three dimensions around the injection site. As shown in Figure 6, the white arrow in each image indicates the injection site, and while the Au and Pd signals radiate out from the injection site, the spreading is not uniform. We predicted that the nanozyme might spread out in the tissue after entering blood vessels in the tumor, but we observed no correlation between Fe and Au signal (Figure S12), suggesting very little entry into the bloodstream. Instead, it seems that the nanozymes simply diffuse in the tumor tissue in a non-uniform manner.

The quantitative sub-organ distributions of polymeric nanomaterials can also be determined. As an example, guanidinium functionalized polyoxanorborneneimide (PONI) polymers, which can deliver proteins directly into the cytosols of cells,[35,36] were conjugated with DOTA ligated metal mass tags, as described recently,[34] and assembled with DOTA ligated mass-tagged green fluorescent proteins (GFP) and injected into mice. The polymers were conjugated with Tb metal ions, and GFP was conjugated with Tm metal ions. The quantitative distributions of Tm and Tb in mice kidneys 30 min after injection were then determined by LA-ICP-MS (Figure 7). The per pixel LOD and LOQ for Tm were 35 and 50 ng/g, respectively, while for Tb the LOD and LOQ were 36 and 52 ng/g. From the images, it is apparent that the polymer and GFP are not perfectly co-localized, suggesting the nanocomposites eventually disassemble *in vivo* and are excreted separately. The images in Figure 7A and B have a low Pearson's correlation coefficient of 0.38. Also, a ratiometric image that considers the ratio of Tm/Tb (i.e. GFP/polymer) indicates that the relative protein and polymer quantities vary across the kidney (Figure 7C). The white color in ratiometric image indicates the regions of the kidney where the concentration ratio of Tm/Tb is the same as the injected ratio of 1.3. The injected ratio of Tm/Tb is primarily found in the outer edges of the kidney section, which corresponds to the cortex (see Figure 7D). The cortex is the region of the kidney where blood filtering begins, and so Tm and Tb ratios that are close to the injected amounts suggest that the assemblies are still intact when they begin to be filtered by the kidney. Other regions of the kidney have different Tm and Tb levels (Table 3), indicating the polymer and protein are excreted separately. Interestingly, the Tb signal has a punctate appearance (Figure 7A), and these spots correspond to glomeruli, which are the primary filtering units in the cortex. There is also a relatively high concentration of Tb in the renal pelvis, which appears blue in the autofluorescence image and is the region of the kidney from which urine flows to the bladder. Relatively high concentrations of Tb in the glomeruli and renal pelvis indicate that the polymer is being removed via urinary excretion. In contrast, the Tm signal is very low in the renal pelvis, which is perhaps not surprising as proteins tend to be too large to pass though the glomerular filter into the renal pelvis. Overall,

these LA-ICP-MS imaging results indicate that the protein is filtered out in a distinct manner from the polymer.

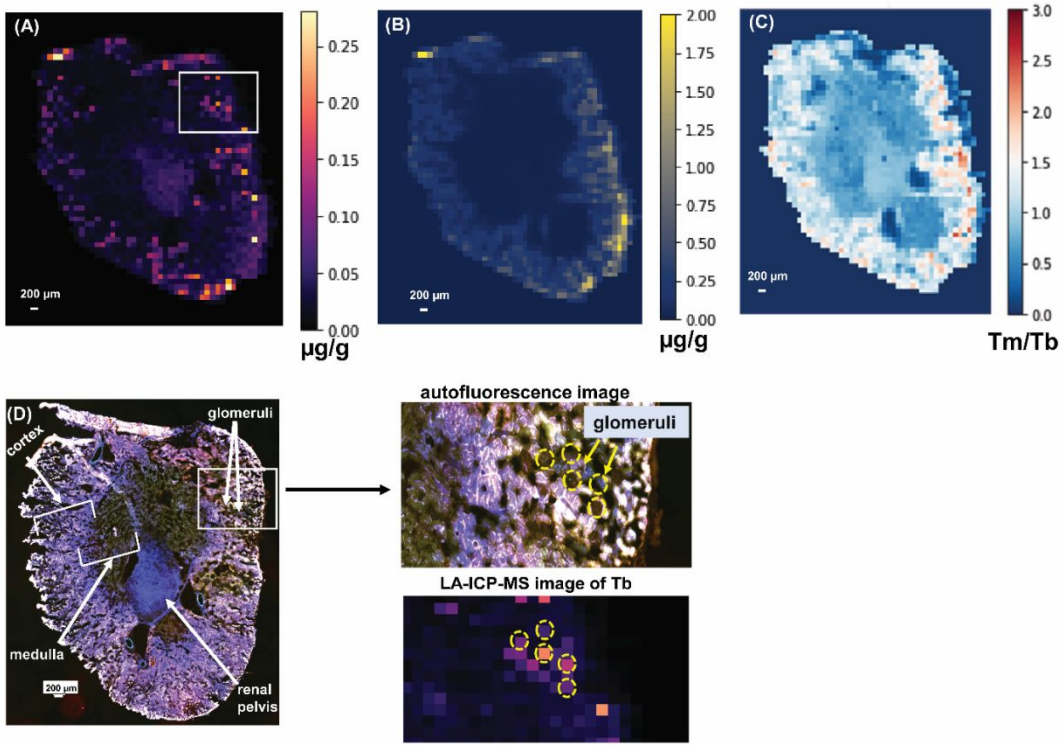

Figure 7. Quantitative LA-ICP-MS and autofluorescence images of a kidney section from a mouse 30 minutes after being injected with polymer-protein nanocomposites consisting of PONI-based polymeric nanomaterials tagged with Tb and GFP tagged with Tm. (A) Quantitative distribution of Tb (PONI polymers). (B) Quantitative distribution of Tm (GFP). (C) Ratiometric image of Tm/Tb (GFP/PONI). (D) Autofluorescence image that reveals the sub-organ regions in the kidney, and the expanded autofluorescence and LA-ICP-MS images of the highlighted rectangular area in the autofluorescence image, showing glomeruli in the kidney.

Table 3. The amount of Tb (PONI polymer) and Tm (GFP) accumulated in the sub-organ regions of the kidney.

Sub-organ region in the kidney	Tb (ng/g)	Tm (ng/g)
Glomeruli	220 ± 20 [a]	300 ± 200 [a]
Cortex	500 ± 200 [a]	650 ± 300 [a]
Renal pelvis	150 ± 5 [a]	- [b]

[a] The error bars are standard deviations (n = 3) that are obtained by averaging the quantitative LA-ICP-MS results obtained from three different tissue sections from a mouse injected with polymer-protein nanocomposites.
[b] The value is below the determine LOD and LOQ of 35 and 50 ng/g, respectively.

Conclusion

In this work, we develop a quantitative LA-ICP-MS imaging platform to determine NM concentrations in sub-organ regions of tissues. Our approach relies on gelatin that is spiked with an internal standard and NM calibration standards and is then placed underneath the tissue of interest and control tissues. Placing control tissues on top of the spiked gelatin standards enables an almost perfect mimic of the biological tissue for calibration purposes. Moreover, utilizing an internal standard (i.e. Ho) improves quantitative precision and allows us to account for signal fluctuations during long LA-ICP-MS imaging experiments. The net result is that we are able to achieve accurate quantitative information of NMs in biological tissues and their sub-organ regions. We illustrate the value of this quantitative imaging approach to determine the sub-organ distributions of positively and negatively-charged AuNPs in the spleen of mice, which provides information about how the different AuNPs interact with the immune system. Such information is not available from measurements of tissue homogenates. We also demonstrate the ability to image the distributions of multiple components associated with complex nanozymes and polymeric nanomaterials, enabling quantitative measures of whether these NM delivery systems remain intact and co-localized *in vivo*. Future implementation of this imaging platform is sure to provide more in-depth information about NM therapeutic delivery systems.

Author Contributions

T.J. and R.W.V. conceptualized the study. T.J., J.D.L., J.D., and D.K.A. performed the experiments. T.J. and J.D.L. analyzed the data. T.J. and R.W.V. wrote the manuscript.

Conflict of interest

The authors declare no competing financial interest.

Acknowledgements

We would like to thank Professor Vincent Rotello and researchers in his group (Xianzhi Zhang and Ritabrita Goswami) at the University of Massachusetts Amherst for the nanoparticle samples. T.J. acknowledges support via a Royal Thai Scholarship from the Development and Promotion of Science and Technology Talents (DPST) Project, Thailand. The work was also supported by a grant (to R.W.V) from the National Science Foundation (CHE-2108044).

References

1 T. Sun, Y. S. Zhang, B. Pang, D. C. Hyun, M. Yang and Y. Xia, *Angew. Chem. Int. Ed.*, 2014, **53**, 12320–12364.

2 K. McNamara and S. A. M. Tofail, *Adv. Phys.: X*, 2017, **2**, 54–88.

3 M. J. Mitchell, M. M. Billingsley, R. M. Haley, M. E. Wechsler, N. A. Peppas and R. Langer, *Nat. Rev. Drug Discovery*, 2021, **20**, 101–124.

4 K. Kenesei, K. Murali, Á. Czéh, J. Piella, V. Puntes and E. Madarász, *J. Nanobiotechnology*, 2016, **14**, 55.

5 R. Lévy, U. Shaheen, Y. Cesbron and V. Sée, *Nano Rev.*, 2010, **1**, 4889.

6 J. C. Waters, *J. Cell Biol.*, 2009, **185**, 1135–1148.

7 P. A. Doble, R. G. de Vega, D. P. Bishop, D. J. Hare and D. Clases, *Chem. Rev.*, 2021, **121**, 11769–11822.

8 J. Chen, R. Wang, M. Ma, L. Gao, B. Zhao and M. Xu, *Anal. Bioanal. Chem.*, 2022, **414**, 7023–7033.

9 Y. Li, W. Guo, Z. Hu, L. Jin, S. Hu and Q. Guo, *J. Agric. Food Chem.*, 2019, **67**, 935–942.

10 D. Hare, C. Austin and P. Doble, *Analyst*, 2012, **137**, 1527–1537.

11 D. J. Hare, J. Lear, D. Bishop, A. Beavis and P. A. Doble, *Anal. Methods*, 2013, **5**, 1915–1921.

12 A. Matusch, A. Bauer and J. S. Becker, *Int. J. Mass Spectrom.*, 2011, **307**, 240–244.

13 D. Pozebon, V. L. Dressler, M. F. Mesko, A. Matusch and J. S. Becker, *J. Anal. At. Spectrom.*, 2010, **25**, 1739–1744.

14 C. Arnaudguilhem, M. Larroque, O. Sgarbura, D. Michau, F. Quenet, S. Carrère, B. Bouyssière and S. Mounicou, *Talanta*, 2021, **222**, 121537.

15 C. Austin, D. Hare, T. Rawling, A. M. McDonagh and P. Doble, *J. Anal. At. Spectrom.*, 2010, **25**, 722–725.

16 H. J. Stärk and R. Wennrich, *Anal. Bioanal. Chem.*, 2011, **399**, 2211–2217.

17 D. J. Bellis and R. Santamaria-Fernandez, *J. Anal. At. Spectrom.*, 2010, **25**, 957–963.

18 M. T. Westerhausen, T. E. Lockwood, R. Gonzalez de Vega, A. Röhnelt, D. P. Bishop, N. Cole, P. A. Doble and D. Clases, *Analyst*, 2019, **144**, 6881–6888.

19 L. J. Castellanos-García, S. Gokhan Elci and R. W. Vachet, *Analyst*, 2020, **145**, 3705–3712.

20 C. Austin, F. Fryer, J. Lear, D. Bishop, D. Hare, T. Rawling, L. Kirkup, A. McDonagh and P. Doble, *J. Anal. At. Spectrom.*, 2011, **26**, 1494–1501.

21 T. Kambe, T. Tsuji, A. Hashimoto and N. Itsumura, *Physiol. Rev.*, 2015, **95**, 749–784.

22 B. Neumann, S. Hösl, K. Schwab, F. Theuring and N. Jakubowski, *J. Neurosci. Methods*, 2020, **334**, 108591.

23 S. Hoesl, B. Neumann, S. Techritz, G. Sauter, R. Simon, H. Schlüter, M. W. Linscheid, F. Theuring, N. Jakubowski and L. Mueller, *J. Anal. At. Spectrom.*, 2016, **31**, 801–808.

24 S. G. Elci, B. Yan, S. T. Kim, K. Saha, Y. Jiang, G. A. Klemmer, D. F. Moyano, G. Y. Tonga, V. M. Rotello and R. W. Vachet, *Analyst*, 2016, **141**, 2418–2425.

25 Y.-K. Hsieh, H.-A. Hsieh, H.-F. Hsieh, T.-H. Wang, C.-C. Ho, P.-P. Lin and C.-F. Wang, *J. Anal. At. Spectrom.*, 2013, **28**, 1396–1401.

26 S. B. Seiffert, A. Vennemann, I. D. Nordhorn, S. Kröger, M. Wiemann and U. Karst, *Chem. Res. Toxicol.*, 2022, **35**, 981–991.

27 N. Grijalba, A. Legrand, V. Holler and C. Bouvier-Capely, *Anal. Bioanal. Chem.*, 2020, **412**, 3113–3122.

28 T. Van Acker, E. Bolea-Fernandez, E. De Vlieghere, J. Gao, O. De Wever and F. Vanhaecke, *J. Anal. At. Spectrom.*, 2019, **34**, 1846–1855.

29 M. Brust, M. Walker, D. Bethell, D. J. Schiffrin and R. Whyman, *J. Chem. Soc., Chem. Commun.*, 1994, 801–802.

30 R. Hong, T. Emrick and V. M. Rotello, *J. Am. Chem. Soc.*, 2004, **126**, 13572–13573.

31 Z.-J. Zhu, P. S. Ghosh, O. R. Miranda, R. W. Vachet and V. M. Rotello, *J. Am. Chem. Soc.*, 2008, **130**, 14139–14143.

32 G. Y. Tonga, Y. Jeong, B. Duncan, T. Mizuhara, R. Mout, R. Das, S. T. Kim, Y.-C. Yeh, B. Yan, S. Hou and V. M. Rotello, *Nat. Chem.*, 2015, **7**, 597–603.

33 X. Zhang, Y. Liu, J. Doungchawee, L. J. Castellanos-García, K. N. Sikora, T. Jeon, R. Goswami, S. Fedeli, A. Gupta, R. Huang, C.-M. Hirschbiegel, R. Cao-Milán, P. K. D. Majhi, Y. A. Cicek, L. Liu, D. J. Jerry, R. W. Vachet and V. M. Rotello, *J. Controlled Release*, 2023, **357**, 31–39.

34 D. K. Agrohia, P. Wu, U. Huynh, S. Thayumanavan and R. W. Vachet, *Anal. Chem.*, 2022, **94**, 7901–7908.

35 R. Goswami, V. Lehot, Y. A. Çiçek, H. Nagaraj, T. Jeon, T. Nguyen, S. Fedeli and V. M. Rotello, *Pharmaceutics*, 2023, 15.

36 Y. W. Lee, D. C. Luther, R. Goswami, T. Jeon, V. Clark, J. Elia, S. Gopalakrishnan and V. M. Rotello, *J. Am. Chem. Soc.*, 2020, **142**, 4349–4355.

37 S. G. Elci, G. Yesilbag Tonga, B. Yan, S. T. Kim, C. S. Kim, Y. Jiang, K. Saha, D. F. Moyano, A. L. M. Marsico, V. M. Rotello and R. W. Vachet, *ACS Nano*, 2017, **11**, 7424–7430.

38 S. G. Elci, Y. Jiang, B. Yan, S. T. Kim, K. Saha, D. F. Moyano, G. Yesilbag Tonga, L. C. Jackson, V. M. Rotello and R. W. Vachet, *ACS Nano*, 2016, **10**, 5536–5542.

39 K. Ovchinnikova, L. Stuart, A. Rakhlin, S. Nikolenko and T. Alexandrov, *Bioinformatics*, 2020, **36**, 3215–3224.

40 L. J. Castellanos-Garcia, K. N. Sikora, J. Doungchawee and R. W. Vachet, *Analyst*, 2021, **146**, 7720–7729.

41 R. E. Mebius and G. Kraal, *Nat. Rev. Immunol.*, 2005, **5**, 606–616.

42 C.-M. Hirschbiegel, X. Zhang, R. Huang, Y. A. Cicek, S. Fedeli and V. M. Rotello, *Adv. Drug Delivery Rev.*, 2023, **195**, 114730.